

See discussions, stats, and author profiles for this publication at: <https://www.researchgate.net/publication/263956115>

Structure and Properties of Novel Cobalt-Free Oxides $NdxSr_{1-x}Fe_0.8Cu_{0.2}O_3-\delta$ ($0.3 \leq x \leq 0.7$) as Cathodes of Intermediate Temperature Solid Oxide Fuel Cells

ARTICLE *in* THE JOURNAL OF PHYSICAL CHEMISTRY C · JUNE 2014

Impact Factor: 4.77 · DOI: 10.1021/jp500371w

CITATIONS

8

READS

22

6 AUTHORS, INCLUDING:



[Yimei Yin](#)

Shanghai Jiao Tong University

29 PUBLICATIONS 269 CITATIONS

[SEE PROFILE](#)



[Chunming Zhang](#)

National Engineering Research Center for Na...

31 PUBLICATIONS 405 CITATIONS

[SEE PROFILE](#)



[Zi-Feng Ma](#)

Shanghai Jiao Tong University

166 PUBLICATIONS 2,463 CITATIONS

[SEE PROFILE](#)

Structure and Properties of Novel Cobalt-Free Oxides $\text{Nd}_x\text{Sr}_{1-x}\text{Fe}_{0.8}\text{Cu}_{0.2}\text{O}_{3-\delta}$ ($0.3 \leq x \leq 0.7$) as Cathodes of Intermediate Temperature Solid Oxide Fuel Cells

Jie-Wei Yin,[†] Yi-Mei Yin,^{*,†} Jun Lu,[†] Chunming Zhang,[‡] Nguyen Q. Minh,[§] and Zi-Feng Ma^{*,†}

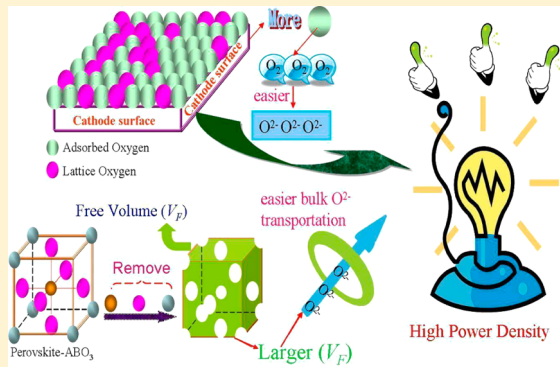
[†]Institute of Electrochemical & Energy Technology, Department of Chemical Engineering, Shanghai Jiao Tong University, Shanghai 200240, PR China

[‡]National Engineering Research Center for Nanotechnology, 28 East Jiangchuan Road, Shanghai 200241, PR China

[§]Center for Energy Research, University of California, San Diego, La Jolla, California 92093-0417, United States

Supporting Information

ABSTRACT: Novel cobalt-free perovskite oxides $\text{Nd}_x\text{Sr}_{1-x}\text{Fe}_{0.8}\text{Cu}_{0.2}\text{O}_{3-\delta}$ (NSFC x , $0.3 \leq x \leq 0.7$) have been prepared and evaluated as cathodes for intermediate temperature solid oxide fuel cells (IT-SOFC). Their structure, thermal expansion, electric, and electrochemical properties are investigated. The oxides exhibit all cubic structure and show excellent thermal and electrochemical performance stability. The Nd content (x) significantly affects the properties of NSCF x . NSFC0.5 has been found to be the optimum composition with a peak electrical conductivity of 124 S cm^{-1} at 700°C , an average thermal expansion coefficient of $14.7 \times 10^{-6} \text{ K}^{-1}$ over 25 – 800°C , a cathodic polarization resistance (R_p) of $0.071 \Omega \text{ cm}^2$ at 700°C , and a peak power density of 900 mW cm^{-2} at 800°C for samarium-doped ceria (SDC)-based single cells with NSFC x cathodes and Ni–SDC anodes. Moreover, no degradation has been observed for the R_p at 700°C within 350 h . The concentration of surface oxygen vacancies and composition dependent crystallographic parameters have been found to be the dominating factors on performance of $\text{Nd}_x\text{Sr}_{1-x}\text{Fe}_{0.8}\text{Cu}_{0.2}\text{O}_{3-\delta}$ as IT-SOFC cathodes.



1. INTRODUCTION

Solid oxide fuel cells (SOFCs) have been developed and considered for a broad spectrum of power generation applications, ranging from watt-size devices to multimegawatt systems. The key attractive features of the SOFC are its clean and efficient production of electricity from a wide range of fuels and its design and manufacturing flexibility.^{1–3} SOFC technology has made significant progress in recent years; however, several critical technical issues, especially those relating to reliability and durability, need to be resolved to move the technology toward commercialization. Current SOFCs operate at high temperatures (800 – 1000°C); the high operating temperature limits material choices for cell and ancillary components, enhances cell performance degradation and elemental interdiffusion between components, and increases sealing difficulties. Therefore, decreasing cell operating temperature to an intermediate range (500 – 800°C) is one approach being considered and evaluated to improve long-term stability, broaden material selection, and reduce sealing issues for the SOFC.^{4,5} However, the electrochemical performance of the SOFC dramatically deteriorates with reduced operating temperature due to increased ohmic resistance of the electrolyte and polarization resistance of the electrodes. In particular, the rapid increase of cathodic polarization resistance with reducing temperature dominantly

contributes to the reduction in cell performance because oxygen reduction kinetics and transport processes at the cathode significantly decrease at lower temperatures due to high activation energy for the oxygen reduction reactions (ORR).

Many efforts have been devoted to develop high-performance cathode materials for intermediate temperature SOFCs (IT-SOFCs). Recently, several cobalt-based mixed conducting perovskite oxides, such as $\text{Ln}_{1-x}\text{Sr}_x\text{CoO}_{3-\delta}$,^{6,7} $\text{Ln}_{1-x}\text{Sr}_x\text{Co}_{1-y}\text{Fe}_y\text{O}_{3-\delta}$,^{8,9} $\text{Ba}_{0.5}\text{Sr}_{0.5}\text{Co}_{0.8}\text{Fe}_{0.2}\text{O}_{3-\delta}$, and $\text{Sm}_{1-x}(\text{Sr}/\text{Ce})_x\text{CoO}_{3-\delta}$,¹¹ have been proposed and studied as cathode materials for IT-SOFCs.^{8,12–14} These materials exhibit excellent catalytic reactivity for oxygen reduction and possess high electronic conductivity in the intermediate temperature range. However, cobalt-based cathodes suffer from high cost and serious performance degradation in long-term operation due to their performance instability and thermal mismatching with electrolytes. These drawbacks originate from facile reduction and easy evaporation of cobalt cations.^{15,16} Cobalt-free perovskite materials have attracted much attention as potential cathodes for IT-SOFCs due to their good electrocatalytic activity and

Received: January 13, 2014

Revised: June 3, 2014

chemical and dimensional stability.^{17–23} Among various cobalt-free materials, copper-doped ferrite perovskite oxides $\text{Ln}_x\text{Sr}_{1-x}\text{Fe}_{1-y}\text{Cu}_y\text{O}_{3-\delta}$ ($\text{Ln} = \text{La}, \text{Pr}, \text{Sm}, \text{and Ba}$) have been considered as one of promising candidates of cathode because of their superior kinetics for the electrocatalytic-reduction of oxygen (i.e., low area specific resistances or ASRs).²⁴ For example, ASRs of $\text{La}_{0.6}\text{Sr}_{0.4}\text{Fe}_{0.8}\text{Cu}_{0.2}\text{O}_{3-\delta}$,²⁰ $\text{Sm}_{0.5}\text{Sr}_{0.5}\text{Fe}_{0.8}\text{Cu}_{0.2}\text{O}_{3-\delta}$,²⁵ and $\text{Pr}_{0.5}\text{Sr}_{0.5}\text{Fe}_{0.8}\text{Cu}_{0.2}\text{O}_{3-\delta}$ ²⁶ cathodes are 0.306, 0.085, and 0.050 $\Omega \text{ cm}^2$ at 700 °C, respectively. It has also been reported²⁷ that the Cu–Fe pair at the B-site of lanthanum transition metal perovskites showed more rapid oxygen mobility than Co–Fe pair and that incorporation of copper into the perovskite structure lowered the sintering temperatures required for electrode fabrication.²⁴ Moreover, copper cations are less evaporative than cobalt cations in perovskite oxides because the bonding energy of Cu–O is stronger than that of Co–O, which may be beneficial to the stability of the $\text{Ln}_x\text{Sr}_{1-x}\text{Fe}_{1-y}\text{Cu}_y\text{O}_{3-\delta}$ perovskite structure.^{28,29}

Although many properties of the $\text{Ln}_x\text{Sr}_{1-x}\text{Fe}_{0.8}\text{Cu}_{0.2}\text{O}_{3-\delta}$ perovskite result from their B-site cations, these properties are also tuned by A-site cations, including the ratio of divalent/trivalent cations and cation size.³⁰ Partial substitution of Sr^{2+} (1.44 Å) by Ba^{2+} (1.61 Å), La^{3+} (1.36 Å), Pr^{3+} (1.30 Å), and Sm^{3+} (1.24 Å) at A-site has been reported to produce cathode materials for IT-SOFCs with excellent electronic conductivity and catalytic activity for the ORR. It has been reported that, among cobalt-based perovskites $\text{Ln}_{0.4}\text{Sr}_{0.6}\text{Fe}_{0.2}\text{Co}_{0.8}\text{O}_{3-\delta}$ ($\text{Ln} = \text{La}, \text{Pr}, \text{Nd}, \text{Sm}, \text{and Gd}$), the one with $\text{Ln} = \text{Nd}$ exhibits the highest electrical conductivity and the best catalytic activity for oxygen reduction,³¹ and the maximum electrical conductivity of $\text{Ln}_x\text{Sr}_{1-x}\text{Fe}_{1-y}\text{Cu}_y\text{O}_{3-\delta}$ has been found to occur at 20% copper dopant, which is assumed due to attainment of the percolation threshold for copper site conduction.^{24,32} Therefore, in the present work, oxides with fixed B-site composition $\text{Nd}_x\text{Sr}_{1-x}\text{Fe}_{0.8}\text{Cu}_{0.2}\text{O}_{3-\delta}$ ($\text{NSFC}_x, 0.3 \leq x \leq 0.7$) were selected for study. The effects of Nd concentration (x) on crystal structure, electrical conductivity, thermal expansion, and electrochemical performance of $\text{Nd}_x\text{Sr}_{1-x}\text{Fe}_{0.8}\text{Cu}_{0.2}\text{O}_{3-\delta}$ were systematically investigated and evaluated from the structure point of view to improve the understanding on the relationship of composition-structure–property of the oxides and provide useful information to design new cathode material for IT-SOFCs.

2. EXPERIMENTAL SECTION

2.1. Material Preparation. $\text{Nd}_x\text{Sr}_{1-x}\text{Fe}_{0.8}\text{Cu}_{0.2}\text{O}_{3-\delta}$ ($\text{NSFC}_x, 0.3 \leq x \leq 0.7$) powders were synthesized via an EDTA-citric acid sol–gel combustion method. The stoichiometric metal nitrates $\text{Nd}(\text{NO}_3)_3 \cdot 6\text{H}_2\text{O}$, $\text{Sr}(\text{NO}_3)_2$, $\text{Fe}(\text{NO}_3)_3 \cdot 9\text{H}_2\text{O}$, and $\text{Cu}(\text{NO}_3)_2 \cdot 3\text{H}_2\text{O}$ were dissolved in EDTA–ammonia solution (pH = 6–7) followed by the addition of citric acid, wherein the molar ratio of total metal ions:EDTA:citric acid was 1:1:2. The solutions were heated at 90 °C under stirring to evaporate the water until purple gels formed. The gels were kept at 250 °C overnight forming black precursors. The precursors were subsequently calcined at 1000 °C for 3 h in air to yield the final desired products denoted as NSFC_x ($x = 0.3, 0.4, 0.5, 0.6, \text{ and } 0.7$).

$\text{Sm}_{0.2}\text{Ce}_{0.8}\text{O}_{1.9}$ (SDC) powders were also synthesized using the sol–gel method and calcined at 750 °C for 5 h.

2.2. Material Characterization. The Goldschmidt tolerance factor t was calculated assuming that copper cations were

mainly bivalence and iron cations were aliovalence, described as follows:

$$t = \frac{r_{\text{A}} + r_{\text{O}}}{\sqrt{2}(r_{\text{B}} + r_{\text{O}})} \quad (1)$$

The radius of cations and anions used in this study were Shannon radii³³ considering the coordination of ions. The oxygen nonstoichiometric values δ of the products at room temperature were determined by iodometric titration.³⁴ X-ray diffraction (XRD) patterns were obtained using X-ray diffractometer (XRD, Rigaku D/max-2200/PC). A Cu K α radiation, $\lambda = 0.15415$ nm was used, and the structure refinement was conducted by the general structure analysis system (GSAS).^{35,36} Brunauer–Emmett–Teller (BET) surface area was determined from N_2 adsorption isotherm with a Micromeritics ASAP 2020 system. X-ray Photoelectron Spectroscopy (XPS) experiments were carried out on a RBD upgraded PHI-5000C ESCA system (PerkinElmer) with Mg K α radiation ($h\nu = 1253.6$ eV) and binding energy was calibrated using the containment carbon ($C_{1s} = 284.6$ eV). The deconvolution of the XPS spectra was completed using the XPS Peak 4.1. Temperature-programmed reduction (TPR) experiments were performed using a Micromeritics AUTO2920-II multicatalyst testing and characterization system, NSFC x (0.20 g) powders were preheated in flowing Ar (20 mL min⁻¹) to 200 °C and held for 2 h, and then after cooling to room temperature reheated in a 10% H_2/Ar mixture (20 mL min⁻¹) at 10 °C min⁻¹ to 1000 °C.

The as-prepared NSFC x powders were ground in an agate mortar to destroy agglomerates, subsequently cold-pressed into bars (20 × 4 × 3 mm) and cylinders (8 mm diameter, 12 mm thickness) at 220 MPa for electrical conductivity and thermal expansion coefficient measurements. The bars and cylinders are sintered at 1160 and 1200 °C in air for 10 h to obtain samples with relative densities all above 90% tested by the Archimedes method. Electrical conductivity of the samples were determined by the 4-point DC terminal method at various temperatures in air, using a Keithley 2420 digital source meter, and a thermal expansion coefficient (TEC) was measured using a dilatometer (NETZSCH DIL 402C) with an Al_2O_3 reference at a heating rate of 5 °C min⁻¹.

2.3. Cell Fabrication and Electrochemical Testing. Symmetrical cells with the configuration of NSFC $x|\text{SDC}|\text{NSFC}x$ were fabricated for impedance studies. SDC electrolyte samples were prepared by pressing SDC powders into pellets and sintered at 1500 °C for 5 h. NSFC x –terpineol–poreformer-based slurries were screen-printed onto both sides of electrolyte samples followed by firing at various temperatures for 2 h. The active area of the applied cathodes was 0.61 cm². Electrode performance was investigated via AC electrochemical impedance spectroscopy (EIS) method using a Zahner IM6eX electrochemical workstation. Applied signals were in the frequency range from 0.01 to 10⁶ Hz and 10 mV amplitude. Impedance data obtained were fitted by Z-View, and cross-sectional microstructures of electrodes after testing with one thermal cycle were examined using field emission-scanning electron microscope (FE-SEM, JSM-7401F). Long-term stability of the cathodes were tested at 700 °C for 350 h in symmetrical cells.

Single cells with configuration of Ni–SDC|SDC|NSFC x were fabricated as follows: the composite anode (NiO + SDC + pore-former) was prepared at 200 MPa as a substrate, and then SDC powder was uniformly distributed onto the substrate, copressed at 250 MPa. The copressed half cells were sintered at 1500 °C for 6 h in air to densify the electrolyte layer. NSFC x cathode slurries

were screen-printed onto the central surface of electrolyte side of the half cells and sintered at 1000 °C for 2 h. The active area of the resulted cathode was about 0.26 cm², and the thickness of electrolyte layer was about 20 μm. Current–voltage (*I*–*V*) curves of single cells were determined using a Keithley 2420 digital source meter. As a comparison, a full cell with a configuration of Ni–YSZ|YSZ|SDC|NSCF0.5 was also fabricated by subsequently screen printed porous SDC buffer layer and NSCF0.5 cathode onto a Ni–YSZ|YSZ commercial half cell (NingBo Institute of Materials Technology & Engineering) and then sintered at 1250 and 1000 °C for 2 h, respectively.

3. RESULTS AND DISCUSSION

3.1. Structural Study. The XRD patterns of $\text{Nd}_x\text{Sr}_{1-x}\text{Fe}_{0.8}\text{Cu}_{0.2}\text{O}_{3-\delta}$ (NSFC x , $0.3 \leq x \leq 0.7$) powders are shown in Figure 1a. It can be seen that all samples are single

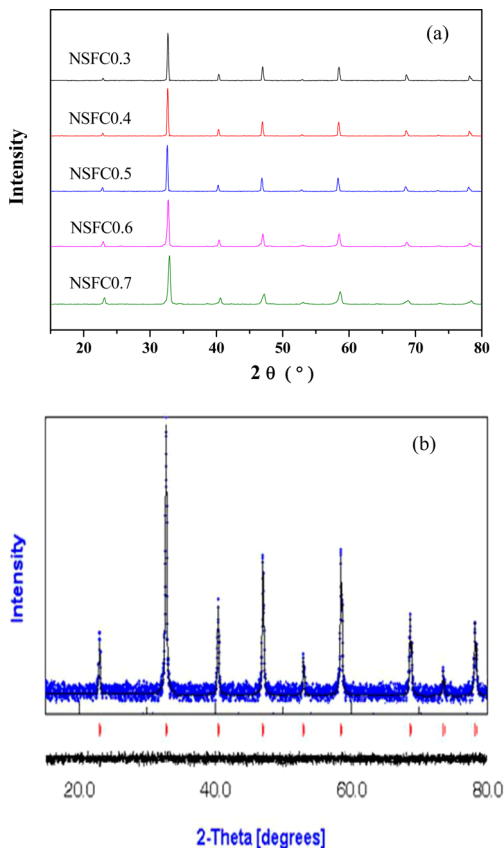


Figure 1. (a) XRD patterns of NSFC x ($0.3 \leq x \leq 0.7$), and (b) Rietveld refinement plots of NSFC0.5.

perovskite phase with nearly cubic structure similar to that of lanthanum ferrite (LaFeO_3). To get more structural information, the lattice structures of NSFC x were further analyzed by GSAS using LaFeO_3 (space group $Pm\bar{3}m$) as an initial model. The calculated results of the final fitting factors and cell parameters of NSFC x are listed in Table 1. Taking NSFC0.5 as a representative (Figure 1b, others in Figure S1 of the Supporting Information), the low reliability factors of $\text{Sig} = 1.229$, $R_w = 3.257\%$, $R_b = 5.307\%$, and $R_{\text{exp}} = 5.298\%$ represent satisfactory refinement results. As can be seen in Table 1, the sample with $x = 0.5$ shows the largest unit cell volume, which may be attributed to the synchronous effect of mean A/B cation size and cation valence changing with the increase of x . For NSFC0.3 and NSFC0.4,

Table 1. Refined Structural Parameters and Final Factors for NSFC x ($0.3 \leq x \leq 0.7$) Determined by the Rietveld Analysis Using GSAS

x	Sig	R_w (%)	R_b (%)	R_{exp} (%)	a (Å)	V (Å ³)
0.3	1.144	3.129	4.725	4.5955	3.8584	57.44
0.4	1.279	3.403	5.552	5.2114	3.8632	57.66
0.5	1.229	3.257	5.307	5.298	3.8639	57.69
0.6	1.612	3.996	5.7972	5.4008	3.8579	57.41
0.7	1.941	4.171	7.195	7.3268	3.8528	57.19

divalent large Sr^{2+} (1.44 Å) cations dominantly exist at the A-site, which causes a severe charge imbalance for the oxides, thus inducing electronic compensation from the valence increase of B-site cations and ionic compensation from the formation of oxygen vacancies. The B-site cations are oxidized to form smaller ions in higher valence ($\text{Fe}^{3+} \rightarrow \text{Fe}^{4+}$ and $\text{Cu}^{2+} \rightarrow \text{Cu}^{3+}$), and thereby strengthen the B–O bond in B–O octahedral according to Pauling's second rule.³⁷ The synergistic effect of the enhanced bond strength, the smaller ions at the B-site, and loss of oxygen is stronger than the effect of large Sr^{2+} at the A-site and, therefore, results in smaller unit cell volumes. Considering the oxygen deficiency (δ) of the materials as listed in Table 2, the mean

Table 2. Relationship of Goldschmidt Tolerance Factor t , Oxygen Deficiency δ , BET Value, and TEC of NSFC x ($0.3 \leq x \leq 0.7$)

x	t	δ	mean A-site cation size (Å)	BET surface area (m ² g ⁻¹)	TEC (10 ⁻⁶ K ⁻¹)
0.3	1.024	0.12	1.389	3.21	16.1
0.4	1.017	0.070	1.372	2.97	15.6
0.5	1.010	0.040	1.355	3.19	14.7
0.6	1.002	0.015	1.338	3.36	14.2
0.7	0.9946	~0	1.321	3.08	14.0

valence state of the B-site cations (V_B) = $0.8V_{\text{Fe}} + 0.2V_{\text{Cu}}$ needs to be equal to $[2(3 - \delta) - V_A]$ (the mean valence state of A-site cations $V_A = [x\text{Nd}^{3+} + (1 - x)\text{Sr}^{2+}]$) to fulfill charge neutrality; therefore, the values of V_B reduced with x and the values are 3.46, 3.46, 3.42, 3.37, and 3.30, respectively, at $x = 0.3, 0.4, 0.5, 0.6$, and 0.7. Although the decreased valence state of the B-site cations with larger ionic size may result in the lattice expansion, the doped Nd with smaller ionic size (Nd^{3+} , 1.27 Å) plays the key role and finally causes the lattice shrinkage at higher Nd^{3+} content as $x = 0.6$ and 0.7. As a result, the unit cell volume of NSFC0.5 exhibits a peak value in the NSFC x . Similar phenomena have previously been observed for other perovskite oxides, such as $\text{La}_{1-x}\text{Sr}_x\text{CoO}_{3-\delta}$ ⁷ and $\text{Pr}_{1-x}\text{Sr}_x\text{Co}_{0.2}\text{Fe}_{0.8}\text{O}_{3-\delta}$.³⁸ The BET values of NSFC x listed in Table 2 show similar values of about 3.0 m² g⁻¹, indicating that x does not remarkably influence the specific surface area of NSFC x .

The oxygen deficiency (δ) of a perovskite oxide is important for its ionic conductivity and catalytic activity for the ORR, while the Goldschmidt tolerance factor (t) gives a hint about the stability of the oxide, and $0.77 \leq t \leq 1.00$ is commonly accepted as a character of stable perovskite structure.^{33,39} Both δ and t of NSFC x are listed in Table 2, columns 2 and 3. As expected, both values decrease with increasing x (Nd^{3+} , 1.27 Å) as a result of the weakening of ionic compensation and the reduction of average A-site cation size, respectively. The negative charge caused by substitution of Sr^{2+} for Nd^{3+} is compensated by a mixed valence of B-site cations ($\text{Fe}^{3+}/\text{Fe}^{4+}$ and $\text{Cu}^{2+}/\text{Cu}^{3+}$) and/or by creation of oxygen vacancies. The high valence cations ($\text{Fe}^{4+} \rightarrow \text{Fe}^{3+}$,

$\text{Cu}^{3+} \rightarrow \text{Cu}^{2+}$) will be thermally reduced at elevated temperatures in the calcining process, and more oxygen vacancies subsequently form corresponding to the decreased coordination of B-site cations. The reoxidation of the oxides during cooling becomes sluggish for higher Sr substitution samples (smaller value of x) and results in an apparent oxygen defect concentration δ at room temperature.⁷ As seen in Table 2 column 3, the t value of NSFC0.6 is mostly close to 1, indicating that the structure of the material has the highest symmetry. Although small deviations of t from 1 for other NSFC x oxides may result in slight tilting of the BO_6 octahedra, the cubic structures are still maintained, as shown in XRD patterns.

The ORR on mixed ionic electronic conductors (MIECs) has been considered as the combination of adsorption–desorption of oxygen molecules at the surface of cathode, formation of oxygen atoms, reduction of oxygen molecules (charge-transfer), incorporation of oxygen ions into cathode materials, transport of oxygen ions within the materials, and injection into the electrolyte.³⁹ Since charge-transfer and incorporation of oxygen ion are facile for MIECs,⁴⁰ surface-exchange process of oxygen species and diffusion of oxide ions within bulk material play important roles in the ORR. X-ray photoelectron spectroscopy (XPS) is a surface sensitive technique and H_2 -temperature-programmed reduction (TPR) can show the information on the reduction of surface species and the stability of the materials. Therefore, XPS and TPR techniques are used to investigate surface species of NSFC x . Surface compositions of NSFC x based on XPS results are summarized in Table 3, and O_{1s} spectra

Table 3. Surface Compositions of NSFC x Perovskite Oxides Identified by XPS

x	(Nd+Sr)/(Cu+Fe)	Nd/(Nd+Sr)	Cu/(Cu+Fe)	O _{ads} /O _{lat}
0.3	1.04	0.12	0.24	1.44
0.4	1.10	0.23	0.22	1.91
0.5	1.13	0.31	0.25	2.31
0.6	0.98	0.38	0.25	1.69
0.7	0.84	0.46	0.32	1.57

analyzed by the curve fitting technique are shown in Figure 2a. As seen in Table 3, the surface of the three samples of $x = 0.3\text{--}0.5$ are enriched by A-site cations (column 2) with respect to B-site cations, and in particular by Sr^{2+} (column 3). Such Sr^{2+} enrichment has often been reported in literature^{41,42} and may be related to the catalytic activity of the oxides.⁴³ However, for $x = 0.7$, an obvious enrichment of B-site cations is observed (column 2, Table 3), which may be ascribed to Cu enrichment at the surface, as the ratio of Cu/(Cu+Fe) is significantly higher than expected for such a composition (column 4, Table 3) and similar enrichment has also been reported for $\text{La}_{0.8}\text{Sr}_{0.2}\text{Cu}_{0.15}\text{Fe}_{0.85}\text{O}_{3-\delta}$.²⁷ One more worth-noting result of XPS is the prominently higher proportion of adsorbed oxygen species (O_{ads}) at the surface of all samples with respect to lattice oxygen (O_{lat}) (column 5, Table 3, and Figure 2a), which suggests easy formation of oxygen vacancies at the surface NSFC x , especially for NSFC0.5 with the largest ratio of O_{ads}/O_{lat} (column 5, Table 3).

The spectra of Fe_{2p} and Cu_{2p} are shown in Figure 2 (panels b and c), respectively. Although the peak positions of Fe 2p (2p_{3/2} at 710.5 eV and 2p_{1/2} at 723.8 eV) are in agreement with the binding energy of Fe (III),^{13,44} the band of the peaks are wide enough to include contribution from Fe⁴⁺ (~712 eV) and Fe³⁺ (~710 eV) oxidation states,¹³ as exhibited by fitted lines of Fe

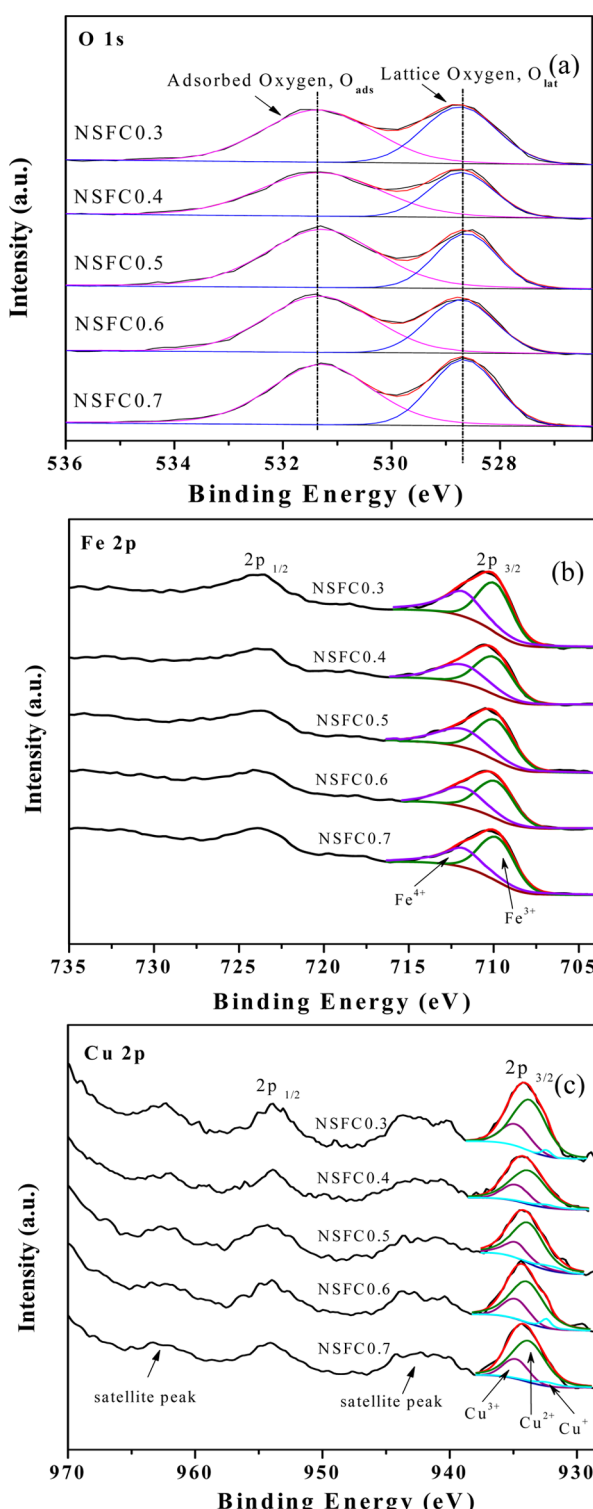


Figure 2. XPS spectra of (a) O 1s, (b) Fe 2p, and (c) Cu 2p for NSFC x ($0.3 \leq x \leq 0.7$).

2p_{3/2}. The peak positions of Cu 2p_{3/2} at 934.2 eV and Cu 2p_{1/2} at 953.9 eV with satellites at 938–946 eV are slightly higher than the reported characteristic of Cu(II) 2p_{3/2} at 933.6 eV,^{45,46} suggesting the possible existence of higher valence of Cu species, mostly possible Cu³⁺. By deconvolution of Cu 2p_{3/2} peaks, three peaks are distinguished, which are attributed to Cu³⁺ (934.6 eV), Cu²⁺ (933.6 eV), and Cu¹⁺ (932.4 eV) oxidation states.⁴⁷ The relative amount of Fe⁴⁺ and Cu³⁺ may not be precise due to the

difficulty in accurately fitting the XPS spectra; anyway, the presence of Fe^{4+} and Cu^{3+} is clearly demonstrated. Moreover, the existence of Fe^{4+} in other perovskites such as $\text{La}_{0.2}\text{Sr}_{0.8}\text{Cu}_{0.4}\text{M}_{0.6}\text{O}_{3-\delta}$ ($\text{M} = \text{Co}$ and Fe)⁴⁸ and $\text{Ba}_{0.95}\text{La}_{0.05}\text{FeO}_{3-\delta}$ ²³ has been directly detected by Mössbauer spectroscopy, and the presence of Cu^{3+} in perovskites has also been proved by X-ray adsorption spectroscopy in $\text{La}_{0.2}\text{Sr}_{0.8}\text{Cu}_{0.4}\text{M}_{0.6}\text{O}_{3-\delta}$ ($\text{M} = \text{Co}$ and Fe)⁴⁸ as well as by neutron diffraction data in $\text{La}_{0.3}\text{Sr}_{0.3}\text{Mn}_{1-x}\text{Cu}_x\text{O}_{3-\delta}$ ($0 \leq x \leq 0.2$)⁴⁹.

The H_2 -TPR profiles over the temperature range of 100–1000 °C are shown in Figure 3a, and two reduction processes are observed for all the oxides. The first reduction peak with the maximum at about 330 °C is ascribed to the reduction from Fe^{4+} to Fe^{3+} and from Cu^{3+} to Cu^{2+} on the surface of the materials,^{50,51} which have been confirmed by XRD with NSFC0.5 as a representative after reduction to the end of the first process at 400 °C, as shown in Figure 3 (panels b and c). No impurity has been found except a shift of the main peak to a lower 2θ value after reduction at 400 °C, showing the expected lattice expansion caused by the reduction of surface B-site cations. The first peak temperature of NSFC x is slightly modified by the substitution of $\text{Nd}^{3+}(x)$. At $x = 0.5$, the peak temperature is the lowest, at 287 °C, revealing that the surface B–O bond of this material is the weakest, therefore, easy to be broken to form oxygen vacancies. It is also suggesting that the oxygen desorption should be easier for NSFC0.5, which may lead to a rapid oxygen surface exchange.⁵² The second peaks with the maximum at about 865 °C are assigned to partial reductions of B-site lattice cations such as Fe^{3+} to Fe^{2+} or Cu^{2+} to Cu^{1+} .^{51,53} The low intensity of the second peaks indicates a low extent of bulk Fe/Cu reduction due to thermal stability of ferrite oxides as documented in the literature.^{53,54} The stability of NSFC x is also verified by XRD on the sample NSFC0.5 before (at 700 °C) and after reduction to the end of the second process at 1000 °C as shown in Figure 3c. As seen, the oxide retains its perovskite structure even at 1000 °C and only trace impurities composed of NdFeO_3 (PDF = 08-0168) and SrNdFeO_4 (PDF = 25-0903) are observed for the sample reduced at 1000 °C except a shift of the peak positions to lower 2θ .

3.2. Electronic Conductivity. The total conductivity of MIECs is the sum of electronic and ionic conductivity, which are closely related to electronic holes and oxygen vacancies. The formation of electronic holes and oxygen vacancies is accomplished by charge compensation for divalent cations such as Sr^{2+} . Electronic compensation through raising the valence of B-site cations forms electronic holes [$\text{B}^{(1+n)+}$, e.g., Fe^{4+} and Cu^{3+}], and ionic compensation forms oxygen vacancies.⁵⁵ Normally, the electronic conductivity is higher than ionic conductivity by about 2–3 orders of magnitude due to very low mobility of oxygen ions comparing to that of electrons, thus the total conductivity is mainly contributed by electronic conductivity. However, the ionic conductivity of MIECs tends to be increased at higher temperatures and high Sr^{2+} substitution due to formation of more oxygen vacancies through partial reduction of $\text{B}^{(1+n)+}$ ($\text{Fe}^{4+}/\text{Cu}^{3+}$) to B^{n+} ($\text{Fe}^{3+}/\text{Cu}^{2+}$) cations.⁵⁶ The conductivities of NSFC x ($0.3 \leq x \leq 0.7$) are plotted as a function of temperature in Figure 4a. As shown, the conductivities of all oxides increase with temperature at lower temperatures below about 700 °C, which is a semiconductor behavior, and then the conductivities decrease with temperature above 700 °C, exhibiting a metallic behavior. The increase of conductivity at lower temperatures is associated with thermal

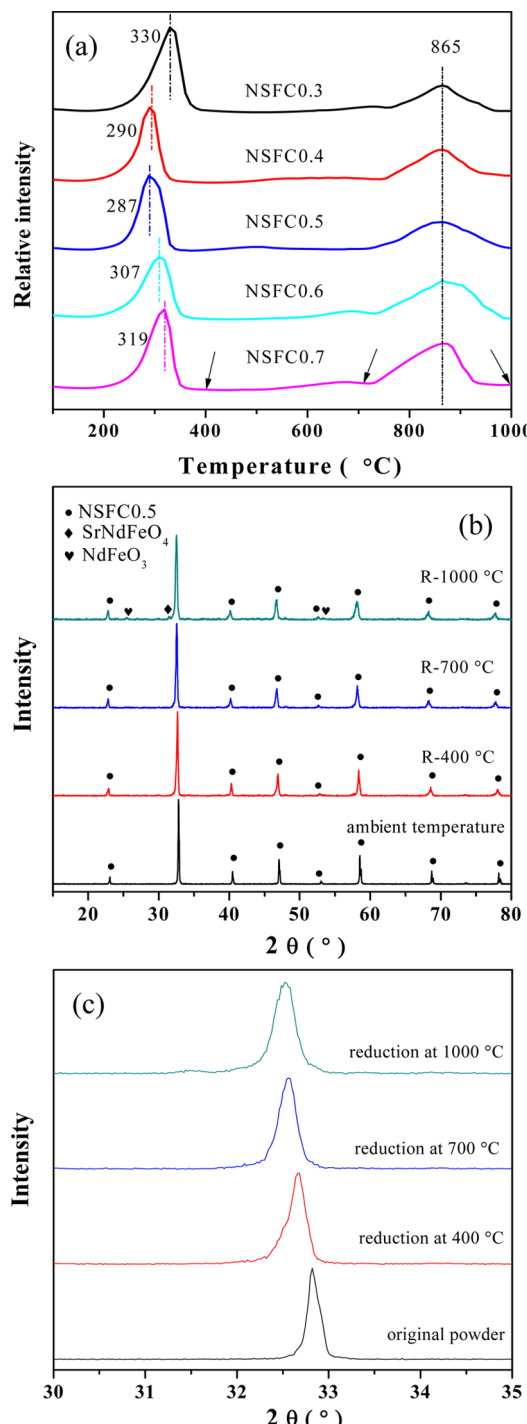


Figure 3. (a) H_2 -TPR profiles of NSFC x ($0.3 \leq x \leq 0.7$) in the temperature range of 100–1000 °C, (b) XRD patterns of NSFC0.5 after exposed to 10% H_2/Ar for 2 h at given temperatures as indicated by arrows in (a), and (c) the enlarged XRD patterns of (b) in the 2θ range of 30–35°.

activated transfer of electrons by hopping through $\text{Fe}^{4+}-\text{O}-\text{Fe}^{3+}$ and $\text{Cu}^{3+}-\text{O}-\text{Cu}^{2+}$ bonds,^{55,57} while the decrease of conductivity above 700 °C is ascribed to the decrease of electronic hole concentration through thermal reduction of Fe^{4+} and Cu^{3+} , as well as the formation of more oxygen vacancies, which also partially remove electronic holes as described by eq 2:⁵⁷

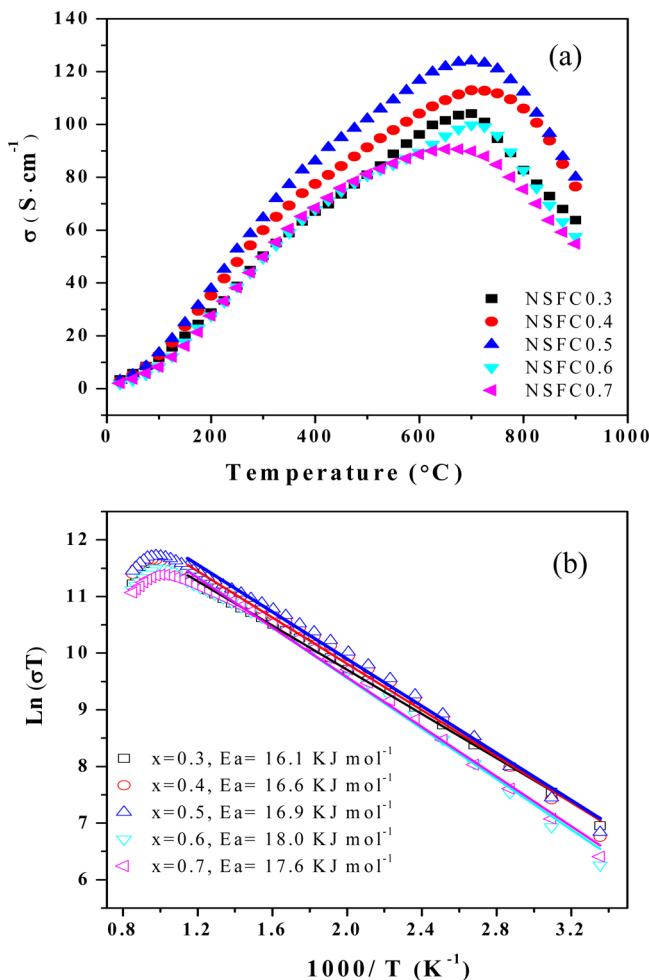
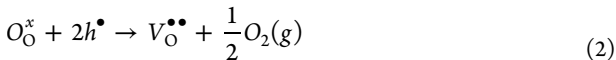


Figure 4. (a) The relationship of electrical conductivity of NSFC x ($0.3 \leq x \leq 0.7$) with temperature and (b) Arrhenius plots of the conductivity for NSFC x ($0.3 \leq x \leq 0.7$).



in which O_O^x is the lattice oxygen, h^\bullet the electronic hole, and V_O^{**} the oxygen vacancy. Similar evolution of conductivity with temperature has been observed in other MIECs such as $Nd_xSr_{1-x}CoO_{3-\delta}$ ⁵⁸ and $La_0.6Sr_0.4Fe_xCu_{1-x}O_{3-\delta}$ ⁵⁹.

NSFC0.5 shows the highest conductivity in temperature range of 100–900 °C with the peak value of 124 S cm $^{-1}$ at 700 °C, which is in agreement with expectation for 50 mol % substitution of divalent cations for trivalent cations at the A-site of perovskite oxides.⁶⁰ In such a case, a maximum $B^{(1+n)+}/B^{n+}$ ratio of 1:1 will be favorable for electron hopping through the $B^{(1+n)+}-O-B^{n+}$ bond in electronic conduction. With decreasing x from 0.7 to 0.5, the conductivity of NSFC x generally increases due to the incremental number of hyper-valence B-site cations for compensating more Sr $^{2+}$ ions. For $x = 0.5 - 0.3$, a further increase in Sr $^{2+}$ concentration induces electrostatic repulsion between hyper-valence Fe $^{4+}$ /Cu $^{3+}$ cations, which may tilt the compensation balance toward formation of oxygen vacancies. Moreover, the increased Fe $^{4+}$ and Cu $^{3+}$ partly play as traps of electrons, thus reduce the number of charge carriers resulting in the decrease of conductivities.

The linear relationship of $\ln(\sigma T)$ with $1/T$ below 700 °C in Arrhenius plots shown in Figure 4b suggests the small polaron

mechanism for the conductivities of NSFC x . The small polaron hopping mechanism can be expressed by eq 3:

$$\sigma = \frac{A}{T} \exp\left(-\frac{E_a}{kT}\right) \quad (3)$$

where A is the pre-exponential factor, T is the temperature, k is the Boltzmann constant, and E_a is the activation energy for small polaron hopping as listed in Figure 4b. The E_a slightly increases with x from 0.3 to 0.6, indicating that more substitution of Nd $^{3+}$ for Sr $^{2+}$ generally makes the hopping of electrons difficult, which is consistent with the literature.^{41,61}

3.3. Thermal Expansion. The thermal expansion curves of NSFC x on heating in air are shown in Figure 5. As comparison,

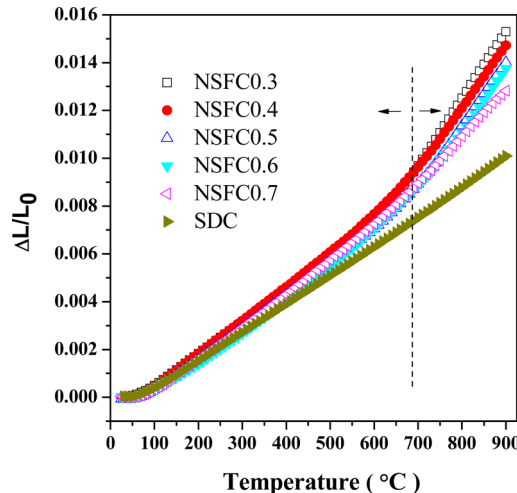


Figure 5. Thermal expansion curves for NSFC x ($0.3 \leq x \leq 0.7$) and SDC under an air atmosphere.

the thermal expansion curve of SDC is also shown in the figure. The curves for NSFC x increase in a linear manner between 100 and 700 °C, caused by thermal expansion of the lattice due to the decrease of electrostatic attractive forces between cations and anions at elevated temperature. The slope of the curves increases at temperatures above around 700 °C because of the additional thermal reduction of B-site cations and the loss of lattice oxygen, which result in a deeper drop of electrostatic attractive forces, and therefore, the greater lattice expansion. The average thermal expansion coefficients (TECs) of NSFC x from room temperature (25 °C) to 800 °C are listed in Table 2. As shown, the TEC generally decreases with increasing x due to the decrease of hyper-valence ions corresponding to the reduction of Sr $^{2+}$ content. NSFC0.5 exhibits a TEC value of 14.7×10^{-6} K $^{-1}$, which is much lower than Co-based materials such as $Ba_{0.5}Sr_{0.5}Co_{0.8}Fe_{0.2}O_{3-\delta}$ (19.7×10^{-6} K $^{-1}$, 30–800 °C)⁶² and $La_{0.6}Sr_{0.4}CoO_{3-\delta}$ (21.3×10^{-6} K $^{-1}$, 50–800 °C),⁹ therefore, matching better with the SDC electrolytes (TEC = 12×10^{-6} K $^{-1}$).⁶³

3.4. Electrochemical Characterization. **3.4.1. Cathodic Performance on Symmetrical Cells.** The performance of NSFC x for the ORR was investigated by EIS analysis based on NSFC x |SDC|NSFC x symmetric cells at 600–800 °C. The typical impedance spectra of symmetric cells at 700 °C are shown in Figure 6a, and the inset is the equivalent circuit for fitting. The intercept of semicircles on real axis at high frequency corresponds to ohmic resistances (R_1) of the cells, while the resistances between the two intercepts on real axis are ascribed to

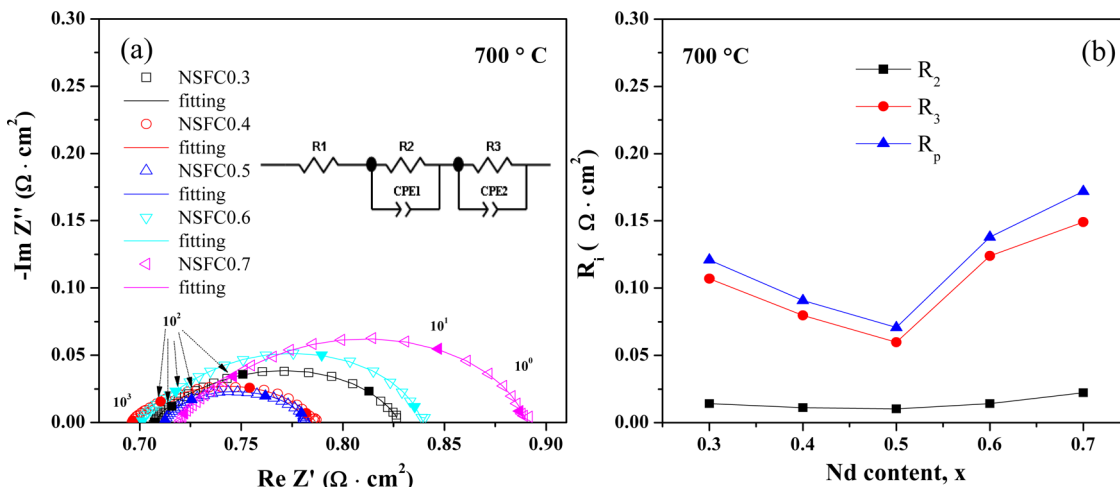


Figure 6. (a) Typical impedance spectra of NSFC_x cathodes at 700 °C under open circuit, the inset is the equivalent circuit adopted for fitting the EIS data. (b) The relationship of fitting results R_i (R_2 , R_3 , and R_p) of NSFC_x cathodes.

polarization resistance R_p . The R_p value is mainly contributed by the resistances from two processes at different frequencies, R_2 and R_3 .⁶⁴ The resistance R_2 at medium frequency ($10^2 \sim 10^4$ Hz) is associated with the charge-transfer process, which includes the ion-transfer occurring at the electrode/electrolyte interface and the electron-transfer at the electrode/current collector interface. The resistance R_3 at low frequency (<10² Hz) is attributed to the nonchemical processes, which includes adsorption–desorption of oxygen, oxygen diffusion within the porous structure of cathode, and diffusion of oxygen ions in the bulk of the cathode.^{64,65} The CPEs indicated in Figure 6a are constant phase elements. The fitting results of the EIS of NSFC_x cathodes at 700 °C are shown in Figure 6b. It can be seen that R_3 dominates R_p with a value much larger than that of R_2 , indicating that the nonchemical process is the rate-determining step for the ORR on NSFC_x at 700 °C. The R_p value first decreases and then increases with x , and NSFC0.5 shows the lowest values at all temperatures (Figure 7), which is consistent with the content of surface oxygen vacancies (see Section 3.1). The specific R_p values are 0.016, 0.032, 0.071, 0.18, and 0.49 Ω cm² at 800, 750, 700, 650, and 600 °C, respectively. The Arrhenius plots of R_p for NSFC_x cathodes measured in air over temperature range of 600–800 °C are

presented in Figure 7. A good linearity of the R_p versus reciprocal temperature is observed, and the derived activation energy ($E_a = 1.38\text{--}1.43$ eV) for the ORR is close to the average of the activation energy of the surface-exchange coefficient and that of the tracer diffusion coefficient (1.01 and 1.79 eV, respectively), which is consistent with the literature.⁶⁶ The values are almost identical for all the samples, indicating that the mechanisms of the ORR are the same for these oxides.

Figure 8 shows the cross-sectional SEM images of tested symmetrical cells. As can be seen from the figure, NSFC_x cathodes show similar porous microstructure and good and continuous contact with the dense SDC electrolyte layer. There are no obvious delamination and cracks at the NSFC_x/SDC interface, suggesting a good compatibility between the cathodes and SDC at tested temperatures.

To further investigate the long-term stability of the NSFC_x cathodes, the evolution of R_p with time for NSFC0.5 as a representative was recorded at 650 and 700 °C, respectively, for 350 h. As shown in Figure 9, the slight fluctuation of the R_p values (± 0.001 and ± 0.003 Ω cm²) can be observed comparing to the average values of 0.070 and 0.181 Ω cm², respectively, for 650 and 700 °C in the test duration, indicating the electrochemical performance of the cathode is very stable.

3.4.2. Single Cell Performances. To further examine the performances of NSFC_x as cathode in IT-SOFCs, anode-supported single cells with SDC as electrolyte in a configuration of NiO–SDC|SDC|NSFC_x were fabricated and tested at 550–800 °C with 50 °C interval. I–V curves of the cells are presented in Figure 10. It can be seen that the open circuit voltages (OCV) of all cells decreases with increasing temperature, which may be ascribed to the reduction of Ce⁴⁺ to Ce³⁺ in the SDC electrolyte at elevated temperatures with subsequent increase in electronic conductivity. The cell with NSFC0.5 as cathode shows the best performances at all tested temperatures; the peak power densities of the cell are 900, 743, 637, 500, 346, and 255 mW cm⁻² at 800, 750, 700, 650, 600, and 550 °C, respectively (Table S1 of the Supporting Information). The excellent performance of Ni–SDC|SDC|NSFC_x single cells is consistent with the cathodic performance of NSFC0.5 in symmetrical cells and suggests that NSFC0.5 is a promising cathode material for IT-SOFCs. Since the introduction of electronic conductivity at raised temperatures in the SDC-based full cells may result in the loss in efficiency due to the leak of electricity, as comparison, a full cell using YSZ as the

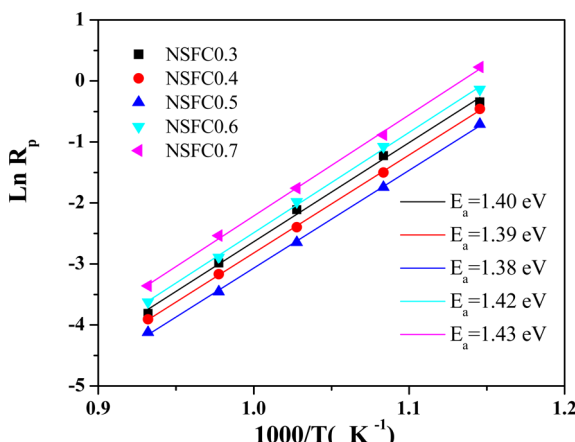


Figure 7. Arrhenius plots of total polarization resistance (R_p) and calculated activation energy (E_a) of NSFC_x cathodes deposited on SDC pellets measured in air under open circuit over a temperature range of 600–800 °C.

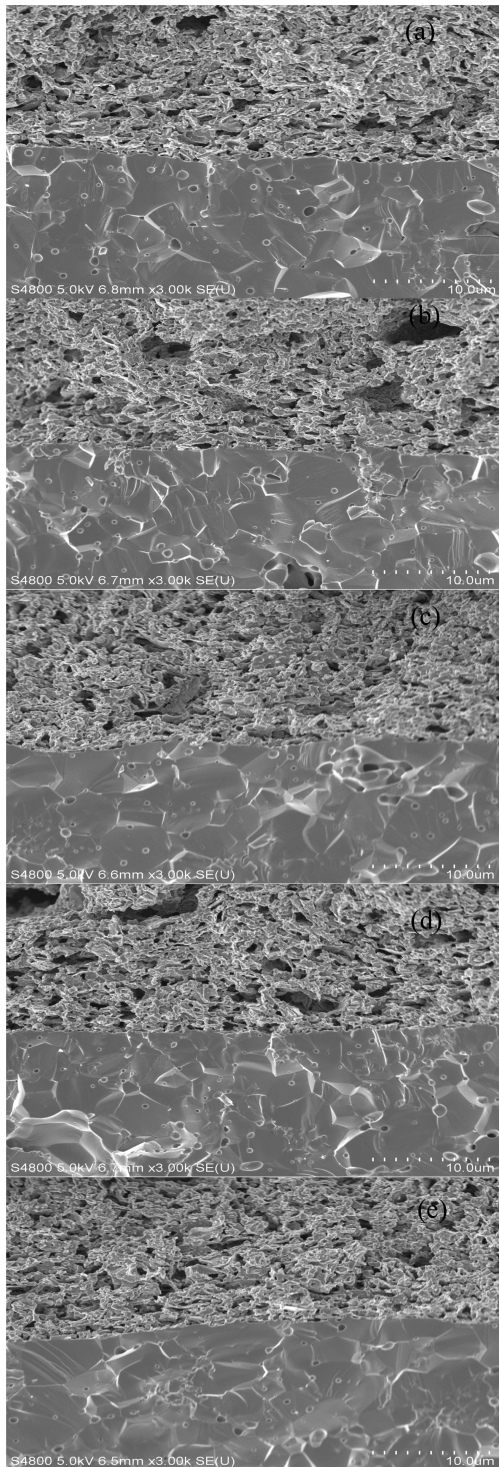


Figure 8. SEM images of cross sections of the NSFC x /SDC interfaces for NSFC x |SDC|NSFC x symmetric cells (a) $x = 0.3$, (b) $x = 0.4$, (c) $x = 0.5$, (d) $x = 0.6$, and (e) $x = 0.7$.

electrolyte, SDC as the buffer layer, and NSFC0.5 as the cathode was also fabricated and examined with a configuration of NiO–YSZ|YSZ|SDC|NSFC0.5 in the temperature range of 550–800 °C; the performances and corresponding impedance spectra are shown in Figure 11. As seen, the performances of NSFCu0.5 in the YSZ-based full cell are comparable to those in the SDC-based full cells. The peak power densities of the cell are 908, 746, 545, 417, 338, and 194 mW cm⁻² at 800, 750, 700, 650, 600, and 550

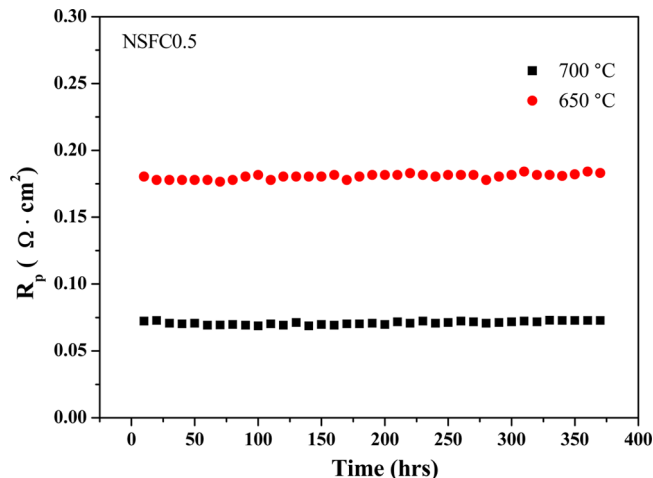


Figure 9. Evolution of polarization resistance (R_p) of NSFC0.5 cathode with time, respectively, at 650 and 700 °C for 350 h.

°C, respectively (Table S1 of the Supporting Information), although the open current voltages of the YSZ-based full cell are higher than those of the SDC-based full cell due to less leak of electricity. It suggests that the performances obtained from the SDC-based full cells can be used in the rapid assessment for the cathode materials.

3.4.3. Reasons for the Difference in NSFC x Cathode Performance. The above results have shown that the cathodic performances of NSFC x are significantly influenced by x , and in addition to the concentration of surface oxygen vacancies (Section 3.1), cathode structure and composition-dependent crystallographic parameters can also contribute to the difference in NSFC x cathode performance. The cross-sectional SEM images of tested symmetrical cells in Figure 8 and Figure S2 of the Supporting Information demonstrate similar microstructure and thickness of the NSFC x cathodes, as well as good adherence between the porous cathode layer and the dense electrolyte, indicating that the structure of the cathode does not significantly contribute to the performance difference.

As mentioned in Cathodic Performance on Symmetrical Cells, the mechanism of the ORR of NSFC x cathodes is governed by adsorption–desorption of oxygen at surface and oxygen ion diffusion in the bulk of cathodes. The oxygen adsorption–desorption at surface of cathode should be easier for NSFC0.5 than any other NSFC x cathodes due to its high content of surface oxygen vacancies and weaker surface B–O bonds as verified by XPS and TPR (in Structural Study). As for migration of oxygen ions in perovskite oxides, it is influenced by crystal structure parameters^{67,68} such as (i) the critical radius (r_c), (ii) the average metal–oxygen bond energy (ABE), and (iii) the lattice free volume (V_F). The critical radius (r_c) represents the radius of the opening between two A-site cations and one B-site cation through which the oxygen ion must pass during diffusion, as shown in the following:

$$r_c = \frac{a_0 \left(\frac{3}{4}a_0 - \sqrt{2}r_B \right) + r_B^2 - r_A^2}{2(r_A - r_B) + \sqrt{2}a_0} \quad (\text{eq } 4)$$

$$a_0 \approx V_{\text{cell}}^{1/3} \quad (\text{eq } 5)$$

in which r_A and r_B are radius of cations at the A-site and B-site, respectively, and a_0 is the lattice parameter.

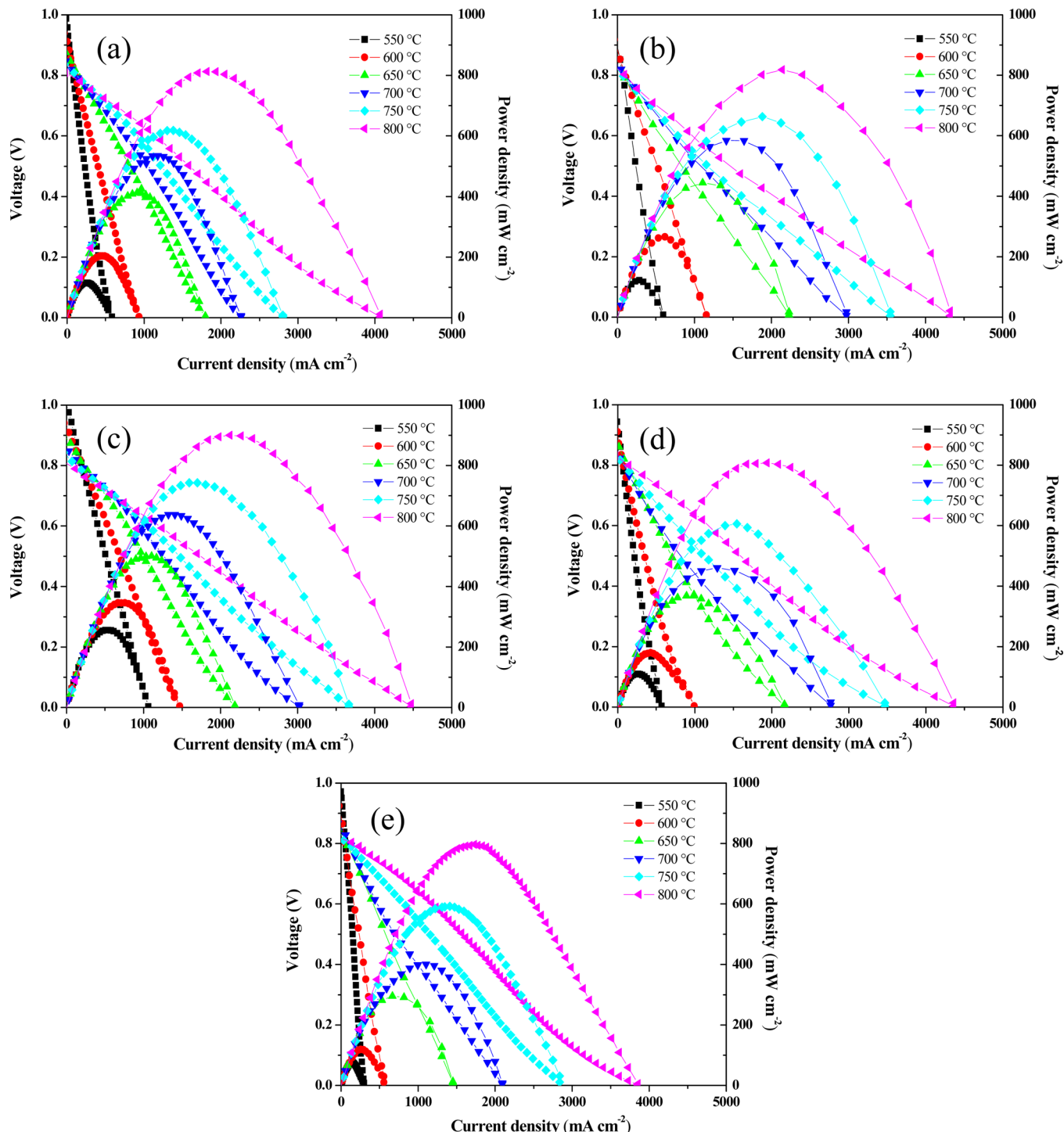


Figure 10. (a–e) Performances of Ni–SDC|SDC|NSFC_x single cells, (a) $x = 0.3$, (b) $x = 0.4$, (c) $x = 0.5$, (d) $x = 0.6$ and (e) $x = 0.7$, using wet hydrogen ($\sim 3\% \text{ H}_2\text{O}$) as fuel and ambient air as oxidant in the temperature range of 550–800 °C.

The average metal–oxygen bond energy (ABE) determine the overall metal–oxygen bond energy in oxides, and weak bond energy will result in facilitation for oxygen ion migration. The average perovskite bond energy can be given by

$$\text{ABE} = \frac{1}{12m} \left(\Delta H_{\text{A}_m\text{O}_n} - m\Delta H_{\text{A}} - \frac{n}{2}D_{(\text{O}_2)} \right) + \frac{1}{6m'} \left(\Delta H_{\text{B}_m\text{O}_n} - m'\Delta H_{\text{B}} - \frac{n'}{2}D_{(\text{O}_2)} \right) \quad (\text{eq } 6)$$

where $\Delta H_{\text{A}_m\text{O}_n}$ and $\Delta H_{\text{B}_m\text{O}_n}$ are the heats of formation of A_mO_n and B_mO_n oxides, ΔH_{A} and ΔH_{B} are the heats of sublimation of the metals A and B, and $D_{(\text{O}_2)}$ is the oxygen dissociation energy (500.2 kJ mol⁻¹).⁶⁹

The lattice free volume (V_F) is defined as the difference between the total unit cell volume and the sum of volumes occupied by the individual ions, as shown below:

$$V_F = a_0^3 - \frac{4}{3}\pi r_A^3 - \frac{4}{3}\pi r_B^3 - \frac{4}{3}(3 - \delta)\pi r_O^3 \quad (\text{eq } 7)$$

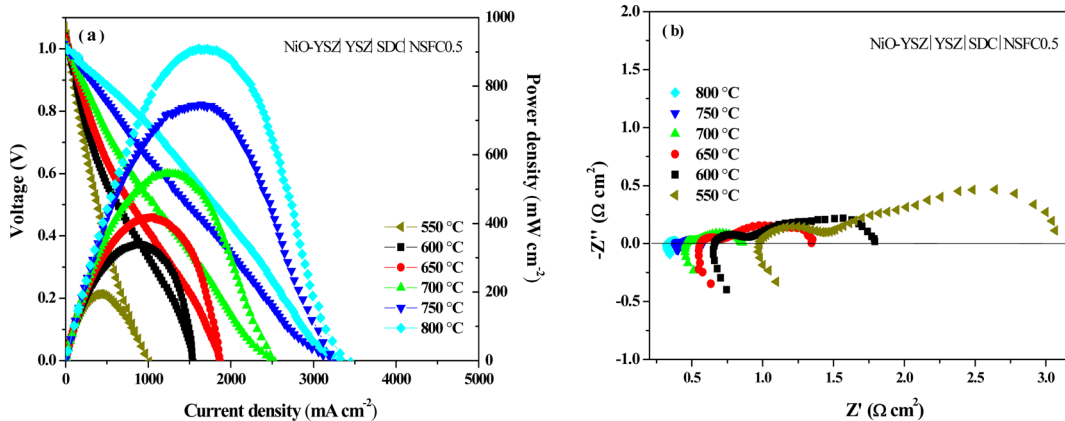


Figure 11. (a) Performances of Ni-YSZ|YSZ|SDC|NSFC0.5, and (b) the corresponding impedance spectra of the cell using wet hydrogen ($\sim 3\%$ H_2O) as fuel and ambient air as oxidant in the temperature range of 550–800 °C.

Table 4. Crystallographic Parameters of NSFC x ($0.3 \leq x \leq 0.7$)

x	r_A or r_B (Å) ³³	ΔH (A_mO_n or B_mO_n) (kJ mol ⁻¹) ⁷⁰	ΔH_A and ΔH_B (kJ mol ⁻¹) ⁷⁰	r_c (Å)	ABE (A-O) (kJ mol ⁻¹)	V_F (Å ³)
0.3	Nd ³⁺ (1.27)	Nd ₂ O ₃ (-1807.9)	327.6	0.88	98.9	11.92
0.4	Sr ²⁺ (1.44)	SrO(-592.0)	164.4	0.89	103.9	11.97
0.5	Fe ³⁺ (0.645)	Fe ₃ O ₂ (-824.2)	416.3	0.90	108.9	12.05
0.6	Cu ²⁺ (0.73)	CuO(-157.3)	337.4	0.91	113.9	11.88
0.7	O ²⁻ (1.40)			0.92	118.9	11.86

in which r_A and r_B are the radii of the A-site and B-site cations, respectively, and δ is the concentration of oxygen vacancies determined by iodometric titration. Generally, the free volume is a “free space” in the lattices, and a larger free volume is believed to be in favor of oxygen ion moving in the lattices.

The three parameters are calculated, assuming Fe and Cu ions mainly adopting 3+ and 2+ valences, respectively, and the calculated results are listed in Table 4. Considering the fixed composition of B-site cations in the bulk of the oxides, the change of r_c and ABE only depend on the Nd and Sr contents at the A-site. As seen, both the values of r_c and ABE monotonically increase with x (columns 5 and 6, Table 4). It has been reported that^{67,68} the ability of oxygen ion migration exhibit a positive correlation with a r_c value and a negative correlation with ABE values. The two competing factors may result in a compromise composition at $x = 0.5$, which is most favorable for oxygen ion migration. As for V_F , NSFC0.5 shows the highest value of 12.05 Å³ (column 7, Table 4), which may be accountable for the best cathodic performance of NSFC0.5 due to easy oxygen ion movement in the larger free volume. Therefore, it is reasonable to believe that the difference of electrochemical performances for NSFC x is related to their intrinsic lattice parameters.

4. CONCLUSIONS

Novel cobalt-free $\text{Nd}_x\text{Sr}_{1-x}\text{Fe}_{0.8}\text{Cu}_{0.2}\text{O}_{3-\delta}$ (NSFC x , $0.3 \leq x \leq 0.7$) have been synthesized, characterized, and evaluated as cathode materials for IT-SOFCs. These oxides exhibit perovskite structure stability in H_2 reducing atmosphere and stable cathode performance in symmetrical cell and single cell tests up to 350 h. The influence of x on properties and performance of the oxides has been examined. The x not only changes surface oxygen vacancy concentration and distribution of A- and B-site cations in NSFC x but also varies intrinsic structure parameters such as critical radius, average metal–oxygen bond energy, and lattice free volume. NSFC0.5 shows the best cathodic performance with the lowest R_p of 0.071 Ω cm² at 700 °C and the highest power

density of 900 mW cm⁻² at 800 °C in single cells of the configuration Ni-SDC|SDC|NSFC x . The analysis and the correlation between composition, structure, and cathode performance of NSFC x indicate that the performance-dominant factors for these materials are surface oxygen vacancies and composition-dependent crystallographic parameters.

ASSOCIATED CONTENT

Supporting Information

Figure S1 shows the Rietveld refinement plots of NSFC x ($0.3 \leq x \leq 0.7$) except for $x = 0.5$. Figure S2 shows the thickness of the cathode layer of NSFC x |SDC|NSFC x symmetric cells. Table S1 summarizes the maximum power densities of NSFC x ($0.3 \leq x \leq 0.7$) at various temperatures. This material is available free of charge via the Internet at <http://pubs.acs.org>.

AUTHOR INFORMATION

Corresponding Authors

*E-mail: yimei@sjtu.edu.cn. Tel: +86 21 34206255. Fax: +86 21 54741297.

*E-mail: zfma@sjtu.edu.cn. Tel: +86 21 54742894. Fax: +86 21 54741297.

Notes

The authors declare no competing financial interest.

ACKNOWLEDGMENTS

This research was financially supported by the Natural Science Foundation of China (Grants 21173147, 21076118, and 21336003), 973 Program of China (Grant 2014CB239700), and the Program of Shanghai Normal University (Grant DZL124). Thanks were also given to the support of National Key Laboratory of Metallic Matrix Composite Material.

REFERENCES

- Minh, N. Q. System Technology for Solid Oxide Fuel Cells. In *Fuel Cell Science and Engineering: Materials, Processes, Systems and Technology*;

- Stolten, D.; Emonts, B., Eds. Wiley-VCH: Hoboken, New Jersey, 2012; Vol. 2, pp 963–1010.
- (2) Steele, B. Appraisal of $\text{Ce}_{1-y}\text{Gd}_y\text{O}_{2-y/2}$ Electrolytes for IT-SOFC Operation at 500° C. *Solid State Ionics* **2000**, *129*, 95–110.
 - (3) Muralidharan, P.; Jo, S. H.; Kim, D. K. Electrical Conductivity of Submicrometer Gadolinia-Doped Ceria Sintered at 1000° C Using Precipitation-Synthesized Nanocrystalline Powders. *J. Am. Ceram. Soc.* **2008**, *91*, 3267–3274.
 - (4) Huijsmans, J.; Van Berkel, F.; Christie, G. Intermediate Temperature SOFC: A Promise for the 21st Century. *J. Power Sources* **1998**, *71*, 107–110.
 - (5) Brett, D. J.; Atkinson, A.; Brandon, N. P.; Skinner, S. J. Intermediate Temperature Solid Oxide Fuel Cells. *Chem. Soc. Rev.* **2008**, *37*, 1568–1578.
 - (6) Dyck, C.; Yu, Z.; Krstic, V. Thermal Expansion Matching of $\text{Gd}_{1-x}\text{Sr}_x\text{CoO}_{3-\delta}$ Composite Cathodes to $\text{Ce}_{0.8}\text{Gd}_{0.2}\text{O}_{1.95}$ IT-SOFC Electrolytes. *Solid State Ionics* **2004**, *171*, 17–23.
 - (7) Mastin, J.; Einarsrud, M.-A.; Grande, T. Structural and Thermal Properties of $\text{La}_{1-x}\text{Sr}_x\text{CoO}_{3-\delta}$. *Chem. Mater.* **2006**, *18*, 6047–6053.
 - (8) Lee, K.; Manthiram, A. $\text{LaSr}_3\text{Fe}_{3-y}\text{Co}_{y10-\delta}$ ($0 \leq y \leq 1.5$) Intergrowth Oxide Cathodes for Intermediate Temperature Solid Oxide Fuel Cells. *Chem. Mater.* **2006**, *18*, 1621–1626.
 - (9) JoongáYoon, K. Enhanced Oxygen Diffusion in Epitaxial Lanthanum–Strontium–Cobaltite Thin Film Cathodes for Micro Solid Oxide Fuel Cells. *Energy Environ. Sci.* **2013**, *6*, 116–120.
 - (10) Shao, Z.; Haile, S. M. A High-Performance Cathode for the Next Generation of Solid-Oxide Fuel Cells. *Nature* **2004**, *431*, 170–173.
 - (11) Yang, W.; Hong, T.; Li, S.; Ma, Z.; Sun, C.; Xia, C.; Chen, L. Perovskite $\text{Sr}_{1-x}\text{Ce}_x\text{CoO}_{3-\delta}$ ($0.05 \leq x \leq 0.15$) as Superior Cathodes for Intermediate Temperature Solid Oxide Fuel Cells. *ACS Appl. Mater. Interfaces* **2013**, *5*, 1143–1148.
 - (12) Smyth, D. M. Perovskite: The Electrically Active Structure. *Ferroelectrics* **2009**, *380*, 1–13.
 - (13) Jin, F.; Shen, Y.; Wang, R.; He, T. Double-Perovskite $\text{PrBaCo}_{2/3}\text{Fe}_{2/3}\text{Cu}_{2/3}\text{O}_{5+\delta}$ as Cathode Material for Intermediate-Temperature Solid-Oxide Fuel Cells. *J. Power Sources* **2013**, *234*, 244–251.
 - (14) Hou, S.-e.; Alonso, J. A.; Rajasekhara, S.; Martínez-Lope, M. a. J. s.; Fernández-Díaz, M. a. T.; Goodenough, J. B. Defective Ni Perovskites as Cathode Materials in Intermediate-Temperature Solid-Oxide Fuel Cells: A Structure–Properties Correlation. *Chem. Mater.* **2010**, *22*, 1071–1079.
 - (15) Wang, H.; Tablet, C.; Feldhoff, A.; Caro, J. A Cobalt-Free Oxygen-Permeable Membrane Based on the Perovskite-Type Oxide $\text{Ba}_{0.5}\text{Sr}_{0.5}\text{Zn}0.2\text{Fe}_{0.8}\text{O}_{3-\delta}$. *Adv. Mater.* **2005**, *17*, 1785–1788.
 - (16) Wei, B.; Lü, Z.; Huang, X.; Liu, M.; Li, N.; Su, W. Synthesis, Electrical and Electrochemical Properties of $\text{Ba}_{0.5}\text{Sr}_{0.5}\text{Zn}_{0.2}\text{Fe}_{0.8}\text{O}_{3-\delta}$ Perovskite Oxide for IT-SOFC Cathode. *J. Power Sources* **2008**, *176*, 1–8.
 - (17) Jiang, S.; Liang, F.; Zhou, W.; Shao, Z. Hierarchical Porous Cobalt-Free Perovskite Electrode for Highly Efficient Oxygen Reduction. *J. Mater. Chem.* **2012**, *22*, 16214–16218.
 - (18) Dong, F.; Chen, Y.; Ran, R.; Chen, D.; Tadé, M. O.; Liu, S.; Shao, Z. $\text{BaNb}_{0.05}\text{Fe}_{0.95}\text{O}_{3-\delta}$ as a New Oxygen Reduction Electrocatalyst for Intermediate Temperature Solid Oxide Fuel Cells. *J. Mater. Chem. A* **2013**, *1*, 9781–9791.
 - (19) Shahgaldi, S.; Yaakob, Z.; Khadem, D. J.; Ahmadrezaei, M.; Daud, W. R. W. Synthesis and Characterization of Cobalt-Free $\text{Ba}_{0.5}\text{Sr}_{0.5}\text{Fe}_{0.8}\text{Cu}_{0.2}\text{O}_{3-\delta}$ Perovskite Oxide Cathode Nanofibers. *J. Alloys Compd.* **2011**, *509*, 9005–9009.
 - (20) Zhou, Q.; Xu, L.; Guo, Y.; Jia, D.; Li, Y.; Wei, W. C. J. $\text{La}_{0.6}\text{Sr}_{0.4}\text{Fe}_{0.8}\text{Cu}_{0.2}\text{O}_{3-\delta}$ Perovskite Oxide as Cathode for IT-SOFC. *Int. J. Hydrogen Energy* **2012**, *37*, 11963–11968.
 - (21) Zhao, L.; He, B.; Zhang, X.; Peng, R.; Meng, G.; Liu, X. Electrochemical Performance of Novel Cobalt-Free Oxide $\text{Ba}_{0.5}\text{Sr}_{0.5}\text{Fe}_{0.8}\text{Cu}_{0.2}\text{O}_{3-\delta}$ for Solid Oxide Fuel Cell Cathode. *J. Power Sources* **2010**, *195*, 1859–1861.
 - (22) Zhou, Q.; He, T.; He, Q.; Ji, Y. Electrochemical Performances of LaBaCuFeO_{5+x} and LaBaCuCoO_{5+x} as Potential Cathode Materials for Intermediate-Temperature Solid Oxide Fuel Cells. *Electrochim. Commun.* **2009**, *11*, 80–83.
 - (23) Dong, F.; Chen, D.; Chen, Y.; Zhao, Q.; Shao, Z. La-doped $\text{BaFeO}_{3-\delta}$ Perovskite as a Cobalt-Free Oxygen Reduction Electrode for Solid Oxide Fuel Cells with Oxygen-Ion Conducting Electrolyte. *J. Mater. Chem.* **2012**, *22*, 15071–15079.
 - (24) Coffey, G. Copper Doped Lanthanum Strontium Ferrite for Reduced Temperature Solid Oxide Fuel Cells. *Solid State Ionics* **2004**, *175*, 73–78.
 - (25) Ling, Y.; Zhao, L.; Lin, B.; Dong, Y.; Zhang, X.; Meng, G.; Liu, X. Investigation of Cobalt-Free Cathode Material $\text{Sm}_{0.5}\text{Sr}_{0.5}\text{Fe}_{0.8}\text{Cu}_{0.2}\text{O}_{3-\delta}$ for Intermediate Temperature Solid Oxide Fuel Cell. *Int. J. Hydrogen Energy* **2010**, *35*, 6905–6910.
 - (26) Lu, J.; Yin, Y.-M.; Ma, Z.-F. Preparation and Characterization of New Cobalt-Free Cathode $\text{Pr}_{0.5}\text{Sr}_{0.5}\text{Fe}_{0.8}\text{Cu}_{0.2}\text{O}_{3-\delta}$ for IT-SOFC. *Int. J. Hydrogen Energy* **2013**, *38*, 10527–10533.
 - (27) Alifanti, M.; Kirchnerova, J.; Delmon, B.; Klvana, D. Methane and Propane Combustion over Lanthanum Transition-Metal Perovskites: Role of Oxygen Mobility. *Appl. Catal., A* **2004**, *262*, 167–176.
 - (28) Kong, X.; Ding, X. Novel Layered Perovskite $\text{SmBaCu}_2\text{O}_{5+\delta}$ as a Potential Cathode for Intermediate Temperature Solid Oxide Fuel Cells. *Int. J. Hydrogen Energy* **2011**, *36*, 15715–15721.
 - (29) Wang, S.-F.; Yeh, C.-T.; Wang, Y.-R.; Hsu, Y.-F. Effects of $(\text{LaSr})(\text{CoFeCu})\text{O}_{3-\delta}$ Cathodes on the Characteristics of Intermediate Temperature Solid Oxide Fuel Cells. *J. Power Sources* **2012**, *201*, 18–25.
 - (30) Attfield, J. Structure–Property Relations in Doped Perovskite Oxides. *Int. J. Inorg. Mater.* **2001**, *3*, 1147–1152.
 - (31) Tu, H.; Takeda, Y.; Imanishi, N.; Yamamoto, O. $\text{Ln}_{0.4}\text{Sr}_{0.6}\text{Co}_{0.8}\text{Fe}_{0.2}\text{O}_{3-\delta}$ ($\text{Ln} = \text{La}, \text{Pr}, \text{Nd}, \text{Sm}, \text{Gd}$) for the Electrode in Solid Oxide Fuel Cells. *Solid State Ionics* **1999**, *117*, 277–281.
 - (32) Kaus, I.; Anderson, H. U. Electrical and Thermal Properties of $\text{La}_{0.2}\text{Sr}_{0.8}\text{Cu}_{0.1}\text{Fe}_{0.9}\text{O}_{3-\delta}$ and $\text{La}_{0.2}\text{Sr}_{0.8}\text{Cu}_{0.2}\text{Fe}_{0.8}\text{O}_{3-\delta}$. *Solid State Ionics* **2000**, *129*, 189–200.
 - (33) Shannon, R. Revised Effective Ionic Radii and Systematic Studies of Interatomic Distances in Halides and Chalcogenides. *Acta Crystallogr., Sect. A* **1976**, *32*, 751–767.
 - (34) Zhang, G.; Dong, X.; Liu, Z.; Zhou, W.; Shao, Z.; Jin, W. Cobalt-Site Cerium Doped $\text{Sm}_{x}\text{Sr}_{1-x}\text{CoO}_{3-\delta}$ Oxides as Potential Cathode Materials for Solid-Oxide Fuel Cells. *J. Power Sources* **2010**, *195*, 3386–3393.
 - (35) Kuroda, C.; Zheng, K.; Świerczek, K. Characterization of Novel $\text{GdBa}_{0.5}\text{Sr}_{0.5}\text{Co}_{2-x}\text{Fe}_x\text{O}_{5+\delta}$ Perovskites for Application in IT-SOFC Cells. *Int. J. Hydrogen Energy* **2013**, *38*, 1027–1038.
 - (36) Toby, B. H. EXPGUI, A Graphical User Interface for GSAS. *J. Appl. Crystallogr.* **2001**, *34*, 210–213.
 - (37) Pauling, L. *The Nature of the Chemical Bond and the Structure of Molecules and Crystals: An Introduction to Modern Structural Chemistry*, 3rd ed.; Cornell University Press: Ithaca, NY: 1960; Vol. 18.
 - (38) Kostoglouidis, G. C.; Ftikos, C. Crystal Structure, Thermal Expansion and Electrical Conductivity of $\text{Pr}_{1-x}\text{Sr}_x\text{Co}_{0.2}\text{Fe}_{0.8}\text{O}_{3-\delta}$ ($0 \leq x \leq 0.5$). *Solid State Ionics* **2000**, *135*, 537–541.
 - (39) Richter, J.; Holtappels, P.; Graule, T.; Nakamura, T.; Gauckler, L. J. Materials Design for Perovskite SOFC Cathodes. *Monatsh. Chem.* **2009**, *140*, 985–999.
 - (40) Armstrong, E. N.; Duncan, K. L.; Wachsman, E. D. Effect of A and B-site Cations on Surface Exchange Coefficient for ABO_3 Perovskite Materials. *Phys. Chem. Chem. Phys.* **2013**, *15*, 2298–308.
 - (41) Yin, Y.-M.; Xiong, M.-W.; Yang, N.-T.; Tong, Z.; Guo, Y.-Q.; Ma, Z.-F.; Sun, E.; Yamanis, J.; Jing, B.-Y. Investigation on Thermal, Electrical, and Electrochemical Properties of Scandium-Doped $\text{Pr}_{0.6}\text{Sr}_{0.4}(\text{Co}_{0.2}\text{Fe}_{0.8})_{(1-x)}\text{Sc}_x\text{O}_{3-\delta}$ as Cathode for IT-SOFC. *Int. J. Hydrogen Energy* **2011**, *36*, 3989–3996.
 - (42) Kirchnerova, J.; Alifanti, M.; Delmon, B. Evidence of Phase Cooperation in the $\text{LaCoO}_3\text{-CeO}_2\text{-Co}_3\text{O}_4$ Catalytic System in Relation to Activity in Methane Combustion. *Appl. Catal., A* **2002**, *231*, 65–80.
 - (43) Gu, H.; Zheng, Y.; Ran, R.; Shao, Z.; Jin, W.; Xu, N.; Ahn, J. Synthesis and Assessment of $\text{La}_{0.8}\text{Sr}_{0.2}\text{Sc}_x\text{Mn}_{1-y}\text{O}_{3-\delta}$ as Cathodes for Solid-Oxide Fuel Cells on Scandium-Stabilized Zirconia Electrolyte. *J. Power Sources* **2008**, *183*, 471–478.

- (44) Yan, A.; Maragou, V.; Arico, A.; Cheng, M.; Tsiaikaris, P. Investigation of a $\text{Ba}_{0.5}\text{Sr}_{0.5}\text{Co}_{0.8}\text{Fe}_{0.2}\text{O}_{3-\delta}$ Based Cathode SOFC II. The Effect of CO_2 on the Chemical Stability. *Appl. Catal., B* **2007**, *76*, 320–327.
- (45) Mathew, T. Cu–Co Synergism in $\text{Cu}_{1-x}\text{Co}_x\text{Fe}_2\text{O}_4$: Catalysis and XPS Aspects. *J. Catal.* **2002**, *210*, 405–417.
- (46) Mathew, T.; Shylesh, S.; Devassy, B. M.; Vijayaraj, M.; Satyanarayana, C. V. V.; Rao, B. S.; Gopinath, C. S. Selective Production of Orthoalkyl Phenols on $\text{Cu}_{0.5}\text{Co}_{0.5}\text{Fe}_2\text{O}_4$: A Study of Catalysis and Characterization. *Appl. Catal., A* **2004**, *273*, 35–45.
- (47) Dai, H. Hole-Doped $\text{La}_{1.85}\text{Sr}_{0.15}\text{CuO}_{4-\delta}\text{X}_\sigma$ ($\text{X}=\text{F}, \text{Cl}$) and Electron-Doped $\text{Nd}_{1.85}\text{Ce}_{0.15}\text{CuO}_{4-\delta}\text{X}_\sigma$ Halo-Oxide Catalysts for the Selective Oxidation of Ethane to Ethene. *J. Catal.* **2001**, *197*, 251–266.
- (48) Genouel, R.; Michel, C.; Nguyen, N.; Studer, F.; Hervieu, M.; Raveau, B. On the Cubic Perovskites $\text{La}_{0.2}\text{Sr}_{0.8}\text{Cu}_{0.4}\text{M}_{0.6}\text{O}_{3-y}$ ($\text{M}=\text{Co}, \text{Fe}$). *J. Solid State Chem.* **1995**, *119*, 260–270.
- (49) Kim, M. S.; Yang, J. B.; Parris, P. E.; Cai, Q.; Zhou, X. D.; James, W. J.; Yelon, W. B.; Buddhikot, D.; Malik, S. K. The Effect of Cu-doping on the Magnetic and Transport Properties of $\text{La}_{0.7}\text{Sr}_{0.3}\text{MnO}_3$. *J. Appl. Phys.* **2005**, *97*, 10H714.
- (50) Chung, J.; Park, J.; Zou, J.; Yoon, H.; Kim, G. Electrochemical Behavior of $\text{Ba}_{0.5}\text{Sr}_{0.5}\text{Co}_{0.2-x}\text{Zn}_x\text{Fe}_{0.8}\text{O}_{3-\delta}$ ($x=0-0.2$) Perovskite Oxides for the Cathode of Solid Oxide Fuel Cells. *Int. J. Hydrogen Energy* **2011**, *36*, 6184–6193.
- (51) Ciambelli, P.; Cimino, S.; De Rossi, S.; Lisi, L.; Minelli, G.; Porta, P.; Russo, G. A FeO_3 ($\text{A}=\text{La}, \text{Nd}, \text{Sm}$) and $\text{LaFe}_{1-x}\text{Mg}_x\text{O}_3$ Perovskites as Methane Combustion and CO Oxidation Catalysts: Structural, Redox and Catalytic Properties. *Appl. Catal., B* **2001**, *29*, 239–250.
- (52) Guo, Y.; Chen, D.; Shi, H.; Ran, R.; Shao, Z. Effect of Sm^{3+} Content on the Properties and Electrochemical Performance of $\text{Sm}_x\text{Sr}_{1-x}\text{CoO}_{3-\delta}$ ($0.2 \leq x \leq 0.8$) as an Oxygen Reduction Electrodes on Doped Ceria Electrolytes. *Electrochim. Acta* **2011**, *56*, 2870–2876.
- (53) Royer, S.; Bérubé, F.; Kaliaguine, S. Effect of the Synthesis Conditions on the Redox and Catalytic Properties in Oxidation Reactions of $\text{LaCo}_{1-x}\text{Fe}_x\text{O}_3$. *Appl. Catal., A* **2005**, *282*, 273–284.
- (54) Ciambelli, P.; Cimino, S.; Lasorella, G.; Lisi, L.; De Rossi, S.; Faticanti, M.; Minelli, G.; Porta, P. CO Oxidation and Methane Combustion on $\text{LaAl}_{1-x}\text{Fe}_x\text{O}_3$ Perovskite Solid Solutions. *Appl. Catal., B* **2002**, *37*, 231–241.
- (55) Li, S. Thermal, Electrical, and Electrochemical Properties of Nd-doped $\text{Ba}_{0.5}\text{Sr}_{0.5}\text{Co}_{0.8}\text{Fe}_{0.2}\text{O}_{3-\delta}$ as a Cathode Material for SOFC. *Solid State Ionics* **2008**, *178*, 1853–1858.
- (56) Dasgupta, N.; Krishnamoorthy, R.; Jacob, T. K. Crystal Structure, Thermal Expansion and Electrical Conductivity of $\text{Nd}_{0.7}\text{Sr}_{0.3}\text{Fe}_{1-x}\text{Co}_x\text{O}_3$ ($0 \leq x \leq 0.8$). *Mater. Sci. Eng., B* **2002**, *90*, 278–286.
- (57) Wei, B.; Lü, Z.; Huang, X.; Miao, J.; Sha, X.; Xin, X.; Su, W. Crystal Structure, Thermal Expansion and Electrical Conductivity of Perovskite Oxides $\text{Ba}_x\text{Sr}_{1-x}\text{Co}_{0.8}\text{Fe}_{0.2}\text{O}_{3-\delta}$ ($0.3 \leq x \leq 0.7$). *J. Eur. Ceram. Soc.* **2006**, *26*, 2827–2832.
- (58) Lee, K. T.; Manthiram, A. Characterization of $\text{Nd}_{1-x}\text{Sr}_x\text{CoO}_{3-\delta}$ ($0 \leq x \leq 0.5$) Cathode Materials for Intermediate Temperature SOFCs. *J. Electrochem. Soc.* **2005**, *152*, A197–A204.
- (59) Ding, X.; Cui, C.; Du, X.; Guo, L. Electrical Conductivity, Thermal Expansion and Electrochemical Properties of Fe-Doped $\text{La}_{0.7}\text{Sr}_{0.3}\text{CuO}_{3-\delta}$ Cathodes for Solid Oxide Fuel Cells. *J. Alloys Compd.* **2009**, *475*, 418–421.
- (60) Bongio, E. V.; Black, H.; Raszewski, F. C.; Edwards, D.; McConville, C. J.; Amaral, V. R. Microstructural and High-Temperature Electrical Characterization of $\text{La}_{1-x}\text{Sr}_x\text{FeO}_{3-\delta}$. *J. Electroceram.* **2005**, *14*, 193–198.
- (61) Pena, M.; Fierro, J. Chemical Structures and Performance of Perovskite Oxides. *Chem. Rev.* **2001**, *101*, 1981–2018.
- (62) Li, Z.; Wei, B.; Lü, Z.; Huang, X.; Su, W. Structure, Electrical and Thermal Properties of $(\text{Ba}_{0.5}\text{Sr}_{0.5})_{1-x}\text{Gd}_x\text{Co}_{0.8}\text{Fe}_{0.2}\text{O}_{3-\delta}$ Perovskite as a Solid-Oxide Fuel Cell Cathode. *Solid State Ionics* **2012**, *207*, 38–43.
- (63) Ding, X.; Kong, X.; Wu, H.; Zhu, Y.; Tang, J.; Zhong, Y. $\text{SmBa}_{0.5}\text{Sr}_{0.5}\text{Cu}_2\text{O}_{5+\delta}$ and $\text{SmBa}_{0.5}\text{Sr}_{0.5}\text{CuFeO}_{5+\delta}$ Layered Perovskite Oxides as Cathodes for IT-SOFCs. *Int. J. Hydrogen Energy* **2012**, *37*, 2546–2551.
- (64) Zhou, W.; Ran, R.; Shao, Z.; Zhuang, W.; Jia, J.; Gu, H.; Jin, W.; Xu, N. Barium- and Strontium-Enriched $(\text{Ba}_{0.5}\text{Sr}_{0.5})_{1+x}\text{Co}_{0.8}\text{Fe}_{0.2}\text{O}_{3-\delta}$ Oxides as High-Performance Cathodes for Intermediate-Temperature Solid-Oxide Fuel Cells. *Acta Mater.* **2008**, *56*, 2687–2698.
- (65) Jørgensen, M. J.; Mogensen, M. Impedance of Solid Oxide Fuel Cell LSM/YSZ Composite Cathodes. *J. Electrochem. Soc.* **2001**, *148*, A433–A442.
- (66) Esquirol, A.; Brandon, N. P.; Kilner, J. A.; Mogensen, M. Electrochemical Characterization of $\text{La}_{0.6}\text{Sr}_{0.4}\text{Co}_{0.2}\text{Fe}_{0.8}\text{O}_3$ Cathodes for Intermediate-Temperature SOFCs. *J. Electrochem. Soc.* **2004**, *151*, A1847–A1855.
- (67) Cook, R. L.; Sammells, A. F. On the Systematic Selection of Perovskite Solid Electrolytes for Intermediate Temperature Fuel Cells. *Solid State Ionics* **1991**, *45*, 311–321.
- (68) Sammells, A. F.; Cook, R. L.; White, J. H.; Osborne, J. J.; MacDuff, R. C. Rational Selection of Advanced Solid Electrolytes for Intermediate Temperature Fuel Cells. *Solid State Ionics* **1992**, *52*, 111–123.
- (69) Li, S.; Jin, W.; Huang, P.; Xu, N.; Shi, J.; Lin, Y.; Hu, M. Z.-C.; Payzant, E. A. Comparison of Oxygen Permeability and Stability of Perovskite Type $\text{La}_{0.2}\text{A}_{0.8}\text{Co}_{0.2}\text{Fe}_{0.8}\text{O}_{3-\delta}$ ($\text{A}=\text{Sr}, \text{Ba}, \text{Ca}$) Membranes. *Ind. Eng. Chem. Res.* **1999**, *38*, 2963–2972.
- (70) Standard Thermodynamic Properties of Chemical Substances. In *CRC Handbook of Chemistry and Physics*, Internet Version 2007, 87th ed.; Lide, D. R., Ed.; Taylor and Francis: Boca Raton, FL, 2007.